Journal of Fluids and Structures 56 (2015) 11–32

Contents lists available at ScienceDirect

Journal of Fluids and Structures

journal homepage: www.elsevier.com/locate/jfs

A multi-physics computational model of fuel sloshing effects on aeroelastic behaviour

J. Hall, T.C.S. Rendall *, C.B. Allen, H. Peel

University of Bristol, Department of Aerospace Engineering, United Kingdom

ARTICLE INFO

Article history:
Received 21 November 2014
Accepted 14 April 2015
Available online 16 May 2015

Keywords:
CFD
Fluid–structure
Numerical modelling
Fuel slosh
Aeroelasticity
Sloshing

ABSTRACT

A multi-physics computational method is presented to model the effect of internally and externally-carried fuel on aeroelastic behaviour of a pitch–plunge aerofoil model through the transonic regime. The model comprises three strongly coupled solvers: a compressible finite-volume Euler code for the external flow, a two-degree of freedom spring model and a smoothed particle hydrodynamics solver for the fuel. The smoothed particle hydrodynamics technique was selected as this brings the benefit that nonlinear behaviour such as wave breaking and tank wall impacts may be included. Coupling is accomplished using an iterative method with subcycling of the fuel solver to resolve the differing timestep requirements. Results from the fuel-structural system are validated experimentally, and internally and externally-carried fuel is considered using time marching analysis. Results show that the influence of the fuel, ignoring the added mass effect, is to raise the flutter boundary at transonic speeds, but that this effect is less pronounced at lower Mach numbers. The stability boundary crossing is also found to be less abrupt when the effect of fuel is included and limit cycles often appear. An external fuel tank is seen to exhibit a lower stability boundary, while the response shows a beating effect symptomatic of two similar frequency components, potentially due to interaction between vertical and horizontal fuel motion.

1. Introduction

Fuel slosh has been shown to be important in the dynamics of a number of vehicle types, including spacecraft (Abramson, 1966; Slabinski, 1978; Vreeburg, 2005; Saturn Flight Evaluation Working Group, 1961), tanker vehicles (Sankar et al., 1992) and ships (Kim et al., 2007). At takeoff, fuel may comprise around 40% of the weight of a large aircraft, while military aircraft may operate with a range of fuel distributions at a wide variety of spanwise hardpoints. Consideration of the influence of fuel motion on loads is therefore critical, and alongside this the influence on aeroelastic motion should be understood. Although the dynamic effect of fuel motion is often assumed to be equivalent to damping, this has only recently been explored numerically. The objective of this work is to develop a multi-physics model to allow determination of the influence of fuel motion for a series of two-dimensional test cases, using more widely applicable modelling assumptions than applied so far, and to a range of larger amplitude motions.

The influence of slosh on rigid body dynamics and control systems has been extensively studied (Bauer, 1963), partly owing to the close correspondence of the sloshing frequencies to those of the controlled body, both with and without gravity (Peterson et al., 1989). For these problems it is important to solve the complete coupled model as dynamic-slosh

* Corresponding author.
E-mail addresses: james.hall@bristol.ac.uk (J. Hall), Thomas.Rendall@bristol.ac.uk (T.C.S. Rendall), C.B.Allen@bristol.ac.uk (C.B. Allen).

http://dx.doi.org/10.1016/j.jfluidstructs.2015.04.003
0889-9746/

interactions can be strong, and lead to a response not predicted from an uncoupled analysis (Peterson et al., 1989). Although the inclusion of elastic effects has been studied to a lesser extent, the effect of fuel slosh on aeroelastic behaviour has been examined previously using computational techniques (Farhat et al., 2013; Firouz-Abadi et al., 2012), applying simplified models such as equivalent mechanical systems (EMS) or hydroelastic models for the fuel, rather than the Euler or Navier–Stokes equations. Ferman and Unger (1979) also extended an analytical model of the fuel motion coupled to panel dynamics and aerodynamics to make estimates for the influence of contained fuel on panel flutter. The hydroelastic model of Farhat et al. (2013) provides a good resolution of fluid behaviour providing that the free surface effects are not large, and can incorporate different boundary conditions and tank designs owing to a finite-element formulation. In comparison, EMS models as applied by Firouz-Abadi et al. (2012) are suitable for stability estimates, but require further simulation in order for the EMS to be constructed accurately for more complicated tank or baffle shapes.

In terms of more detailed modelling, Banim et al. (2006) use smoothed particle hydrodynamics (SPH) to model wing fuel tank sloshing, but applied a forcing function on the wing based on gust loads rather than coupling the solution to an aerodynamic flow solver. An experimental and analytical study on the effect of fuel on flutter was carried out by Sewall (1957), where it was noted that the sequence of emptying of internal fuel tanks is important for the highest flutter onset speed.

Both Farhat et al. (2013) and Firouz-Abadi et al. (2012) conclude that the fuel influence on flutter is usually stabilising, although this cannot be guaranteed for all cases. This is in turn consistent with the experimental results of Merten and Stephenson (1952), who described the damping influence of a tip fuel tank on beam motion, but also noted the variability of the effective fluid mass for dynamic estimates. To examine the possibility of limit cycles and larger amplitude behaviour in more detail an alternative approach for modelling the fuel is required, for which it is useful to consider a meshless method. Smoothed particle hydrodynamics (SPH) has shown promising results for modelling free surface problems, or those with violent motions, primarily as a result of a meshless Lagrangian basis, and compares well to alternative schemes for sloshing (Rebouillat and Liksonov, 2010; Souto-Iglesias et al., 2006). A Lagrangian basis also largely eliminates the meshing bottleneck and eases use for complicated internal geometries, which in turn makes the technique uniquely suited to modelling contained fuel.

Computational progress in engineering has seen the separate development of reliable fluid and structural solvers that are now regularly used within the design cycle (Maman and Farhat, 1995; de Boer et al., 2007; Piperno et al., 1995). Within aeroelastics, monolithic and partitioned approaches have been proposed to cope with the multi-disciplinary nature of the problem. The monolithic approach uses a tailored aero-structural solver (Bendiksen, 1991; Hubner et al., 2004) while the partitioned approach favours the coupling of existing structural and fluid solvers (Woodgate et al., 2005; Lee-Rausch and Batina, 1993; Geuzaine et al., 2003; Djayapertapa and Allen, 2001; Djayapertapa et al., 2001; Taylor et al., 2004; Allen et al., 2005). The partitioned approach is used almost as standard, including within the CFD Group at the University of Bristol (Djayapertapa and Allen, 2001; Djayapertapa et al., 2001; Taylor et al., 2004; Allen et al., 2005), because it allows the use of existing software and grids, but synchronization of the structure and fluid at each time level must be done iteratively (Djayapertapa and Allen, 2001).

A logical step towards higher fidelity is to extend the coupled approach to include the effect of internal fuel through linking to an SPH method. In this work the internal fuel flow is modelled using SPH and the external airflow is governed by the Euler equations, solved on a moving finite volume mesh, while a mechanical spring model is chosen to model the structural behaviour. Use of a full flow solver for the internal fluid allows non-linear effects such as wave breaking to be accounted for, and in future for the inclusion of baffles and more elaborate internal tank designs.

The objective of the work presented here is therefore to couple in a time-accurate fashion three separate solvers, each with their own requirements regarding stability and accuracy. To achieve this a structural-SPH system has been constructed and validated, and a suitable technique for coupling the disparate fluids models is developed and presented here. The method is used to explore the influence of fuel slosh on a flutter boundary for differing fill levels of an internal tank, and for an external (underwing) type tank.

2. Smoothed particle hydrodynamics

Smoothed particle hydrodynamics (SPH) is a meshless, Lagrangian particle based scheme invented independently by Gingold and Monaghan (1977) and Lucy (1977). The technique was originally intended to study problems in astrophysics but has been used for fluids due to the simplicity of using meshless methods to model free surface flows which would otherwise require techniques such as the volume of fluid (VOF) method (Hirt and Nichols, 1981) or alternative schemes to track the free surface and deform the mesh. There are a number of reasons to prefer SPH to VOF; the first is simplicity as no special techniques are required to track free surfaces. The meshless nature of the method also removes the need to create a mesh which can prove challenging in complex geometries. As the SPH method is Lagrangian it also avoids false diffusion errors that can occur in Eulerian methods such as VOF, while the VOF technique also requires solution of a differential equation that describes the evolution of the volume fraction in the mesh volumes.

2.1. Formulation of fuel model

There are two approaches for producing SPH formulations of the governing equations. The first, more generally used, views SPH as a method of representing any given function by summation over a set of particles. Liu and Liu (2005) give

details of the mathematics, but the process is to take a function that approximates the Dirac delta function and convolve it with the function to be represented as in Eq. (1). The angle brackets denote the integral representation, and the objective is to approximate $\nabla p/\rho$ in order to be able to integrate forward (in inviscid flow) $D\mathbf{u}/Dt = -\nabla p/\rho$. The process starts with an integral representation

$$\langle f(\mathbf{x})\rangle = \int_{\Omega} f(\mathbf{x}')W(\mathbf{x}-\mathbf{x}', h)\, d\mathbf{x}'. \tag{1}$$

Here $f(\mathbf{x})$ is a function to be represented by integration over a volume Ω, $W(\mathbf{x}-\mathbf{x}', h)$ is a smoothing function that depends on the difference between the location of interest and the points over which the integral is evaluated. h is a characteristic length of W and is known as the smoothing length. As Price (2012) shows Eq. (1) is second order accurate providing W is symmetric and normalised to give $\int_{\mathbf{x}} W\, d\mathbf{x} = 1$, which may be seen from expanding (assuming gradients of f are known)

$$\langle f(\mathbf{x})\rangle = \int_{\Omega} \left[f(\mathbf{x}) + \frac{\partial f}{\partial \mathbf{x}}(\mathbf{x}'-\mathbf{x}) + \frac{\partial^2 f}{\partial \mathbf{x}^2}(\mathbf{x}'-\mathbf{x})^2 + \cdots \right] W(\mathbf{x}-\mathbf{x}', h)\, d\mathbf{x}'. \tag{2}$$

Symmetry implies that the second term in integral, being antisymmetric, must vanish to leave the second order term as the lead contribution.

This integral representation is then approximated by summation over N nearby particles, shown in Eq. (3). This summation is possible because W is usually chosen to be a compact function which is non-zero only for a small fraction of the total domain. The radius over which W is non-zero is known as the smoothing length or support radius, thus N is the number of particles within the support radius

$$\langle f(\mathbf{x})\rangle \approx \sum_{j=1}^{N} f(\mathbf{x}_j)W(\mathbf{x}-\mathbf{x}_j, h)\Delta V_j. \tag{3}$$

In replacing the integral with a discrete summation, additional errors are incurred that depend on how closely the discrete system satisfies the normalisation and symmetry requirements (Price, 2012), so that

$$\begin{aligned}\langle f(\mathbf{x})\rangle \approx f(\mathbf{x}) \sum_{j=1}^{N} W(\mathbf{x}-\mathbf{x}_j, h)\Delta V_j + \frac{\partial f}{\partial \mathbf{x}} \sum_{j=1}^{N} (\mathbf{x}_j-\mathbf{x}) W(\mathbf{x}-\mathbf{x}_j, h)\Delta V_j \\ + \frac{\partial^2 f}{\partial \mathbf{x}^2} \sum_{j=1}^{N} (\mathbf{x}_j-\mathbf{x})^2 W(\mathbf{x}-\mathbf{x}_j, h)\Delta V_j + \cdots\end{aligned} \tag{4}$$

Ideally it would be true that $\sum \Delta V_j W(\mathbf{x}-\mathbf{x}_j) = 1$ and $\sum \Delta V_j(\mathbf{x}_j-\mathbf{x})W(\mathbf{x}-\mathbf{x}_j) = 0$, but this depends on the particle distribution. In practice, this means that the order of accuracy of the method is dependent on the particle spacing within the smoothing length. Second order accuracy is only retained if the particles are evenly distributed within the smoothing length, in much the same way as central difference finite volume schemes only retain their second order accuracy on smoothly stretching meshes.

If each particle is assigned a mass and a density then Eq. (3) can be written as

$$\langle f(\mathbf{x})\rangle \approx \sum_{j=1}^{N} \frac{m_j}{\rho_j} f(\mathbf{x}_j) W(\mathbf{x}-\mathbf{x}_j, h). \tag{5}$$

Derivatives can be approximated in the same way

$$\langle \nabla f(\mathbf{x})\rangle = \int_{\Omega} \nabla f(\mathbf{x}')W(\mathbf{x}-\mathbf{x}', h) d\mathbf{x}'. \tag{6}$$

However, while the derivative of f may not be known the derivative of the smoothing function is, so the following identity may be applied:

$$\nabla[f(\mathbf{x}')W(\mathbf{x}-\mathbf{x}', h)] = \nabla f(\mathbf{x}')W(\mathbf{x}-\mathbf{x}', h) + f(\mathbf{x}')\nabla W(\mathbf{x}-\mathbf{x}', h). \tag{7}$$

Hence

$$\langle \nabla f(\mathbf{x})\rangle = \int_{\Omega} \nabla[f(\mathbf{x}')W(\mathbf{x}-\mathbf{x}', h)] - f(\mathbf{x}')\nabla W(\mathbf{x}-\mathbf{x}', h) d\mathbf{x}'. \tag{8}$$

And by applying the divergence theorem the first volume integral becomes a surface integral over the problem domain S,

$$\langle \nabla f(\mathbf{x})\rangle = \int_{S} f(\mathbf{x}')W(\mathbf{x}-\mathbf{x}', h) d\mathbf{S} - \int_{\Omega} f(\mathbf{x}')\nabla W(\mathbf{x}-\mathbf{x}', h) d\mathbf{x}'. \tag{9}$$

Usually the support domain is entirely within the problem domain such that the surface integral is zero (as $W=0$ at the edge of the support) and the representation can be expressed entirely in terms of the volume integral. This is not true in the case where the support domain overlaps the boundary (either a free surface or a fixed boundary).

The particle approximation can then be performed to give

$$\langle \nabla f(\mathbf{x}_i)\rangle \approx -\sum_{j=1}^{N} \frac{m_j}{\rho_j} f(\mathbf{x}_j)\nabla W(\mathbf{x}_i-\mathbf{x}_j,h). \tag{10}$$

Note that in Eq. (10) the gradient of the kernel on the right hand side is evaluated at the *j*th particle and as most smoothing functions are symmetric (*this is required for second order accuracy*) Eq. (10) can equivalently be written as Eq. (11), where the subscript *i* denotes evaluating the gradient at the *i*th particle. The sign changes as for a symmetric kernel the gradient will be antisymmetric.

With this information it is possible to construct the governing equations in the SPH formulation to give

$$\langle \nabla f(\mathbf{x}_i)\rangle \approx \sum_{j=1}^{N} \frac{m_j}{\rho_j} f(\mathbf{x}_j)\nabla_i W(\mathbf{x}_i-\mathbf{x}_j,h). \tag{11}$$

Using

$$\frac{\nabla p}{\rho} = \nabla\left(\frac{p}{\rho}\right) + \frac{p}{\rho^2}\nabla\rho, \tag{12}$$

gives

$$\begin{aligned}\frac{\nabla p}{\rho} &\approx -\sum_{j=1}^{N} m_j\left[\frac{p_j}{\rho_j^2}\right]\nabla_i W_{ij} - \sum_{j=1}^{N} m_j\left[\frac{p_i}{\rho_i^2}\right]\nabla_i W_{ij}\\ &= -\sum_{j=1}^{N} m_j\left[\frac{p_j}{\rho_j^2}+\frac{p_i}{\rho_i^2}\right]\nabla_i W_{ij},\end{aligned} \tag{13}$$

where on the right hand side, $f=p/\rho$ and $f=\rho$ can be identified and used to construct the approximation from Eq. (11). Alternative identities can be employed giving different formulations to Eq. (13) (Price, 2012).

At present the SPH formulation used is

$$W_{ij} = \frac{7}{4\pi h^2}\left(1-\frac{|\mathbf{x}_i-\mathbf{x}_j|}{2h}\right)^4\left(2\frac{|\mathbf{x}_i-\mathbf{x}_j|}{h}+1\right), \quad \frac{|\mathbf{x}_i-\mathbf{x}_j|}{h}\le 2, \tag{14}$$

$$\frac{D\mathbf{u}_i}{Dt} = -\sum_{j=1}^{N} m_j\left[\frac{p_j}{\rho_j^2}+\frac{p_i}{\rho_i^2}\right]\nabla_i W_{ij} + \sum_{j=1}^{N} m_j \nu \frac{\rho_i+\rho_j}{\rho_i\rho_j}\frac{\mathbf{x}_{ij}\cdot\nabla_i W_{ij}}{|\mathbf{x}_{ij}|^2+0.001h^2}\mathbf{u}_{ij}+\mathbf{g}, \tag{15}$$

$$\frac{D\rho_i}{Dt} = \sum_{j=1}^{N} m_j(\mathbf{u}_i-\mathbf{u}_j)\cdot\nabla_i W_{ij}, \tag{16}$$

$$p = B\left(\left(\frac{\rho}{\rho_0}\right)^{\gamma}-1\right). \tag{17}$$

Eq. (14) is the quintic kernel suggested by Wendland (1995). The equation of state, Eq. (17), is commonly used in SPH to remove the need to solve a pressure Poisson equation, and an equation of this form was first suggested by Cole (1948) for water, before Monaghan (1994) then suggested setting B such that the speed of sound in the fluid is an order of magnitude greater than the fastest particle velocity. γ here is set to 7 following Cole's (1948) work. This is known as the weakly compressible method, and is able to predict free surface motion (Monaghan, 1994; Lee et al., 2008). The second term in Eq. (15) is a viscosity term proposed by Morris et al. (1997) which helps prevent non-physical particle interpenetration.

The question of how to deal with boundary conditions in SPH is complex and a number of schemes exist. Monaghan (1988) suggests three ways of enforcing a rigid boundary:

1. Forces of length scale equal to the smoothing length.
2. Reflecting particles that cross the boundary without energy loss.
3. Fixing particles on the boundary to provide a repulsive force.

In this paper the third method has been used with the modification that the solid boundary particles are fixed only relative to the others in that rigid body. Force and moment on a rigid body are therefore calculated by summing the contribution from each of the solid boundary particles.

2.2. Time integration

The Newmark-beta method (Huebner et al., 1995) with $\gamma=1/2$, $\beta=1/4$ (these constants give the constant average acceleration integration and a scheme that is unconditionally stable) is used to time integrate the SPH code by applying it to

Eqs. (15) and (16) (where $\ddot{\mathbf{s}} = D\mathbf{u}/Dt$):

$$\dot{\mathbf{s}}^{t+\Delta t} = \dot{\mathbf{s}}^{t} + (1-\gamma)\Delta t\ddot{\mathbf{u}}^{t} + \gamma\Delta t\ddot{\mathbf{s}}^{t+\Delta t}, \tag{18}$$

$$\mathbf{s}^{t+\Delta t} = \mathbf{s}^{t} + \Delta t\dot{\mathbf{s}}^{t} + \frac{1-2\beta}{2}\Delta t^2\ddot{\mathbf{s}}^{t} + \Delta t^2\beta\ddot{\mathbf{s}}^{t+\Delta t}. \tag{19}$$

The Newmark-beta method is implicit, so the particle acceleration and density rate of change from Eqs. (15) and (16) are substituted into Eqs. (18) and (19) to perform the time integration, and fixed point iteration carried out to converge to a solution for time level $n+1$.

3. Aeroelastic model

The objective of this work is to explore the chordwise/pitching influence of fuel on the aeroelastic system. Although for a real aircraft wing spanwise fuel motion is important, for clarity and to enable comparison to established results, this complexity is not incorporated for this analysis. A two degree of freedom model still models the pitch–plunge flutter behaviour, and can incorporate the consequences of pitch and plunge motions on the fuel. Isogai's (1980) model, previously used for calculating flutter boundaries via linear stability and CFD methods, is adopted where the governing coupled differential equations are given by Eq. (20) and parameters illustrated in Fig. 1:

$$\begin{bmatrix} m & S \\ S & I_\alpha \end{bmatrix}\begin{pmatrix} \ddot{y} \\ \ddot{\alpha} \end{pmatrix} + \begin{bmatrix} K_y & 0 \\ 0 & K_\alpha \end{bmatrix}\begin{pmatrix} y \\ \alpha \end{pmatrix} = \begin{pmatrix} L \\ M \end{pmatrix}. \tag{20}$$

Here m is the mass of the wing (kg/m), S the static imbalance (kg), I_α the moment of inertia (kg m) about the elastic axis, K_y the plunge spring stiffness (N/m/m), K_α the pitching spring stiffness (N) and L and M are the vertical force and pitching moment about the elastic axis respectively. L is positive upwards and M is positive nose up.

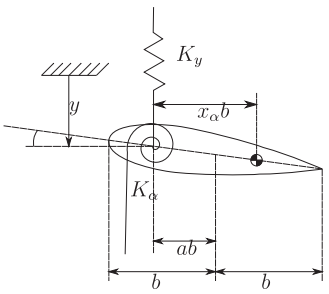

Fig. 1. Structural model.

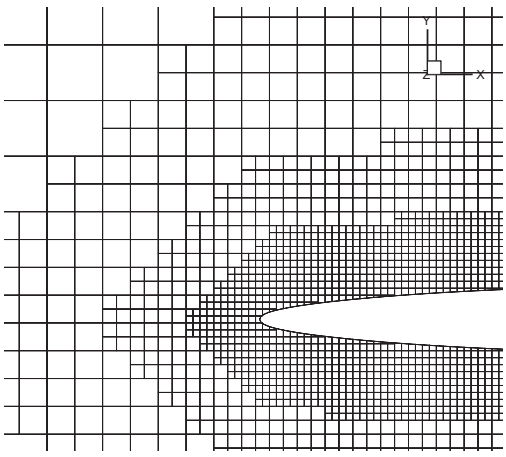

Fig. 2. Detail of cut-cell mesh near boundary.

This system is usually expressed in a non-dimensional form given by (Alonso and Jameson, 1994)

$$\begin{bmatrix} 1 & x_\alpha \\ x_\alpha & r_\alpha^2 \end{bmatrix} \begin{pmatrix} \ddot{h} \\ \ddot{\alpha} \end{pmatrix} + \begin{bmatrix} \left(\frac{\omega_h}{\omega_\alpha}\right)^2 & 0 \\ 0 & r_\alpha^2 \end{bmatrix} \begin{pmatrix} h \\ \alpha \end{pmatrix} = \frac{S_i^2}{\pi} \begin{pmatrix} C_l \\ 2C_m \end{pmatrix}. \tag{21}$$

Here dots rather than dashes denote the derivative with respect to non-dimensional time $\tau = \omega_\alpha t$. The non-dimensional parameters are as defined by Isogai (1979) and are

- The mass ratio $\mu = m/\pi\rho b^2$, which expresses the ratio of section mass to the mass of air.
- Non-dimensional static imbalance $x_\alpha = S/mb$, indicating the level of pitch–plunge inertial coupling.

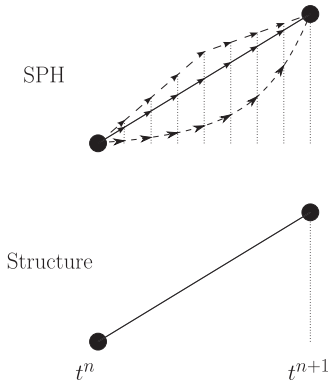

Fig. 3. Substep process.

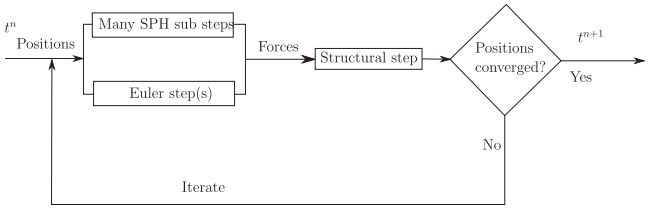

Fig. 4. Coupling process.

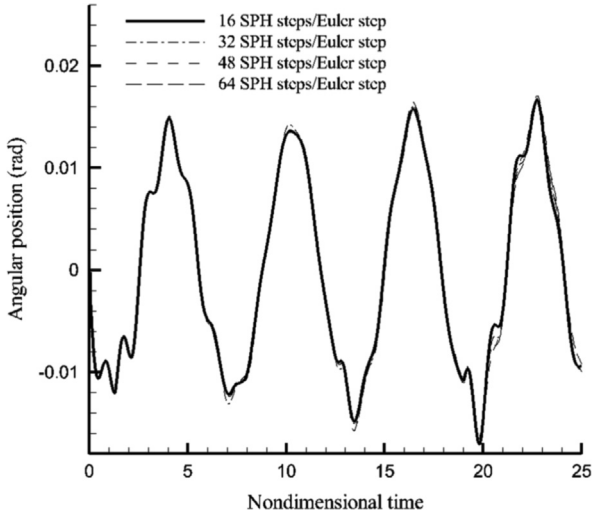

Fig. 5. Comparison of time histories for varying Euler timesteps (legend indicates the number of SPH timesteps per Euler timestep, where SPH timestep is held fixed, $M=0.85$, speed index$=0.95$).

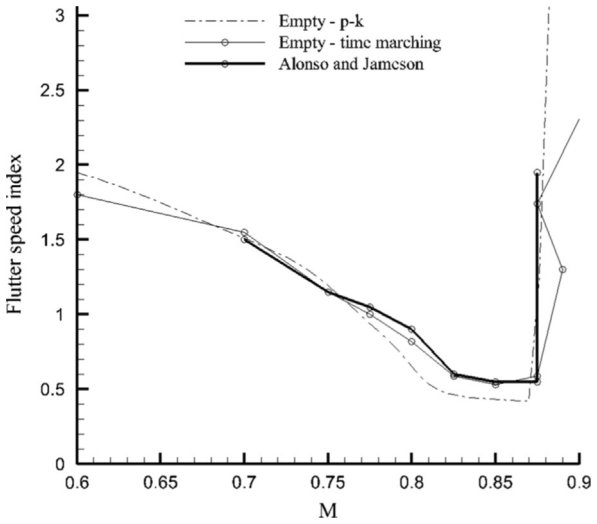

Fig. 6. Flutter boundary comparison.

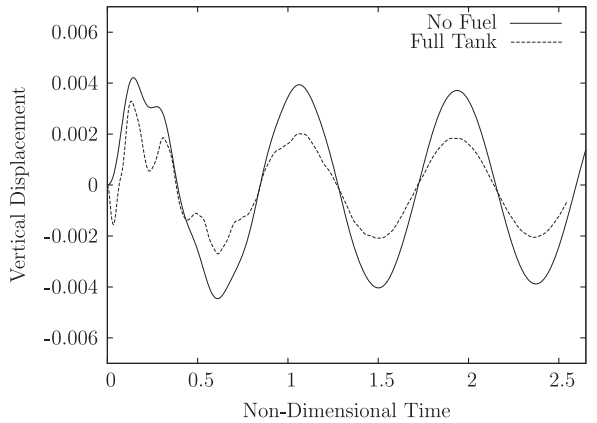

Fig. 7. Comparison between full and empty fuel tank including the effect of external aerodynamics, at M=0.75 with speed index=1.03, slosh index=7.18.

- The non-dimensional radius of gyration $r_\alpha = \sqrt{I_\alpha/mb^2}$.
- Speed index $S_i = 1/k_c\sqrt{\mu}$, which gives the ratio of aerodynamic to stiffness forces.
- Reduced frequency $k_c = \omega_\alpha b/U_\infty$, which implies the level of aerodynamic unsteadiness.

The Newmark-beta scheme, also used for the SPH integration, is used for time integration of the structure. It is useful to rearrange Eq. (21) for the accelerations in terms of the positions at time $t+\Delta t$ and then substitute this into Eq. (19) to solve for the positions; the accelerations and velocities can then be simply found.

It has been shown (Piperno and Farhat, 2001) in aeroelastic calculations where the external flow and structure are simulated that energy conservation has a large impact on the accuracy of aeroelastic stability predictions as any energy loss acts as a damper and a gain acts as negative damping. It may also be shown that given an energy conserving time integrator (such as the Newmark scheme), the global energy of a system consisting of a rigid body represented by boundary SPH particles and a fluid is conserved if the force and moment on the rigid body are found by summation over the forces on the boundary particles. Hence, total force and moment of the fuel are found here through a summation of forces acting on the boundary particles.

The external flow is governed by an inviscid arbitrary Lagrangian–Eulerian model (Hirt et al., 1974) and solved using a cell-centred, finite volume (Jameson et al., 1981), solver of the Jameson–Schmidt–Turkel type, as shown in Fig. 2. Time integration is implicit in real time using a 2nd order backward difference, but explicit in pseudo-time via a Runge–Kutta integration, and mesh motion is accomplished using a radial basis function method (Rendall and Allen, 2008). In this work a geometry preserving cut-cell mesh is used, with 12 refinement levels from farfield to the surface.

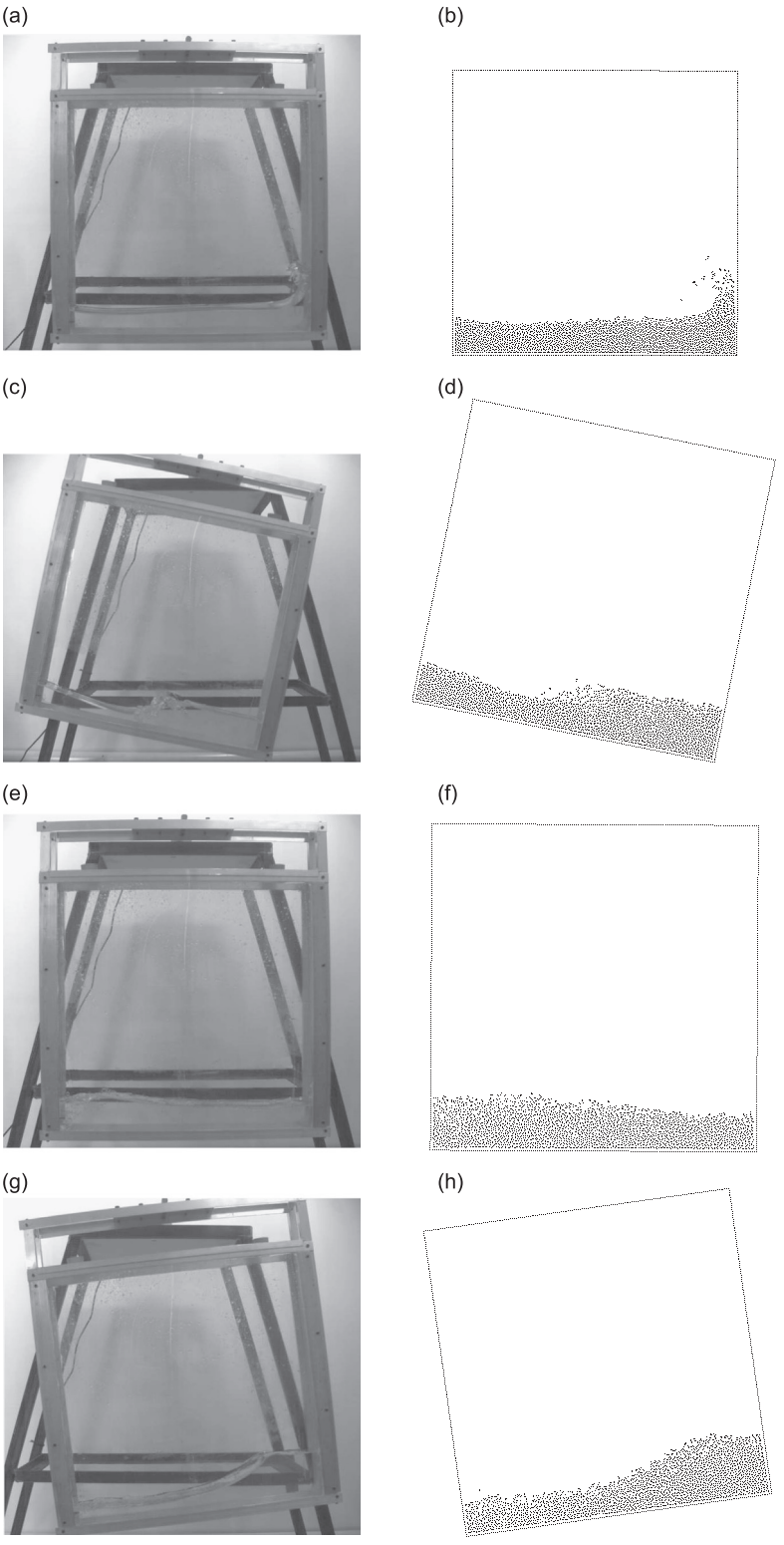

Fig. 8. Comparison of predicted and experimental free surface positions for the sloshing box. (a) $T = 0.229T_\alpha$, (b) $T = 0.229T_\alpha$, (c) $T = 0.758T_\alpha$, (d) $T = 0.758T_\alpha$, (e) $T = 0.758T_\alpha$, (f) $T = 0.758T_\alpha$, (g) $T = 0.954T_\alpha$, (h) $T = 0.954T_\alpha$.

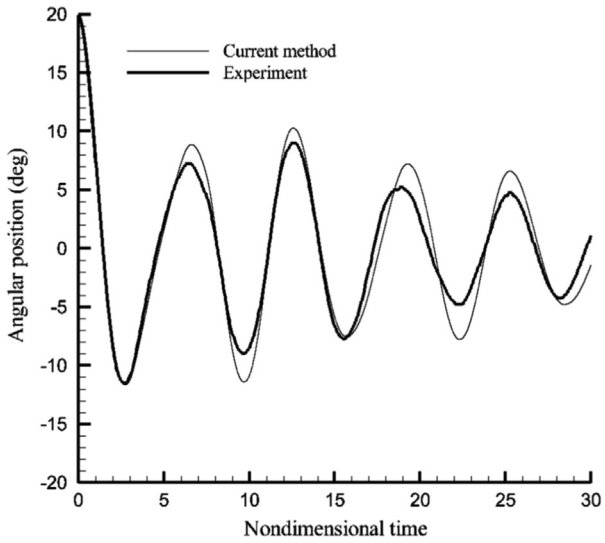

Fig. 9. Comparison of predicted and experimental time histories for angular position of the sloshing box.

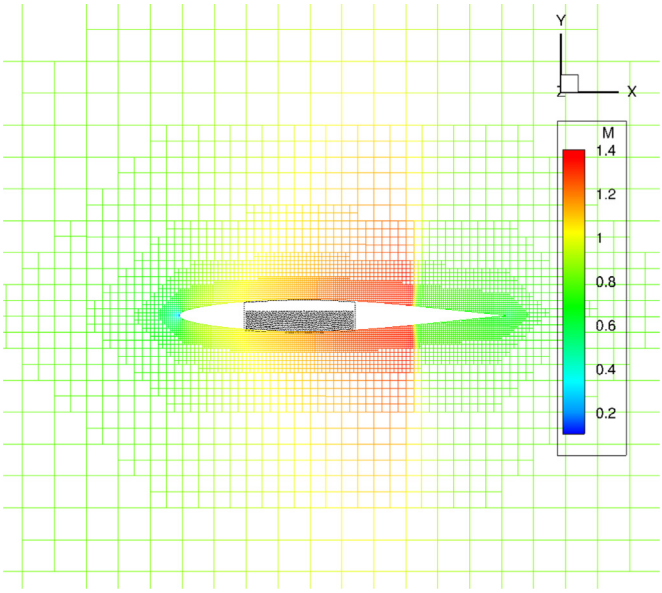

Fig. 10. Initial set up, 67% fill.

4. Inclusion of sloshing and coupling of models

The equation of motion may be modified to include sloshing and again non-dimensionalised using $\tau=\omega_\alpha t$, $\eta=y/b$, $C_f=F/\frac{1}{2}\rho_f g2b(2b)$, $C_g=G/\frac{1}{2}\rho_f g2b(2b)^2$, where F is the vertical force from the fuel and G is the moment (note the deliberate analogy to lift and moment coefficients by replacing dynamic pressure with $\frac{1}{2}\rho_f gh2b$, the hydrostatic head for semi-chord depth), to give

$$\begin{pmatrix} 1 & x_\alpha \\ x_\alpha & r_\alpha^2 \end{pmatrix}\begin{pmatrix} \ddot{\eta} \\ \ddot{\alpha} \end{pmatrix}+f_s\begin{pmatrix} \left(\frac{\omega_h}{\omega_\alpha}\right)^2 & 0 \\ 0 & r_\alpha^2 \end{pmatrix}\begin{pmatrix} \eta \\ \alpha \end{pmatrix} = f_s\frac{S_i^2}{\pi}\begin{pmatrix} C_l \\ 2C_m \end{pmatrix}+f_s\frac{S_f^2}{\pi}\begin{pmatrix} 2C_f \\ 4C_g \end{pmatrix}=\mathbf{F}, \tag{22}$$

where the speed index $S_i=V_\infty/\omega_\alpha b\sqrt{\mu}$, g is the acceleration due to gravity, b is the semi-chord of the wing, the slosh index $S_f=1/\sqrt{\omega_\alpha^2 b/g}\sqrt{\mu_f}$, $f_s=(m+m_f)/m$, $\mu=(m+m_f)/\pi\rho b^2$, $\mu_f=(m+m_f)/\pi\rho_f b^2$ and subscript f denotes fuel quantities. A

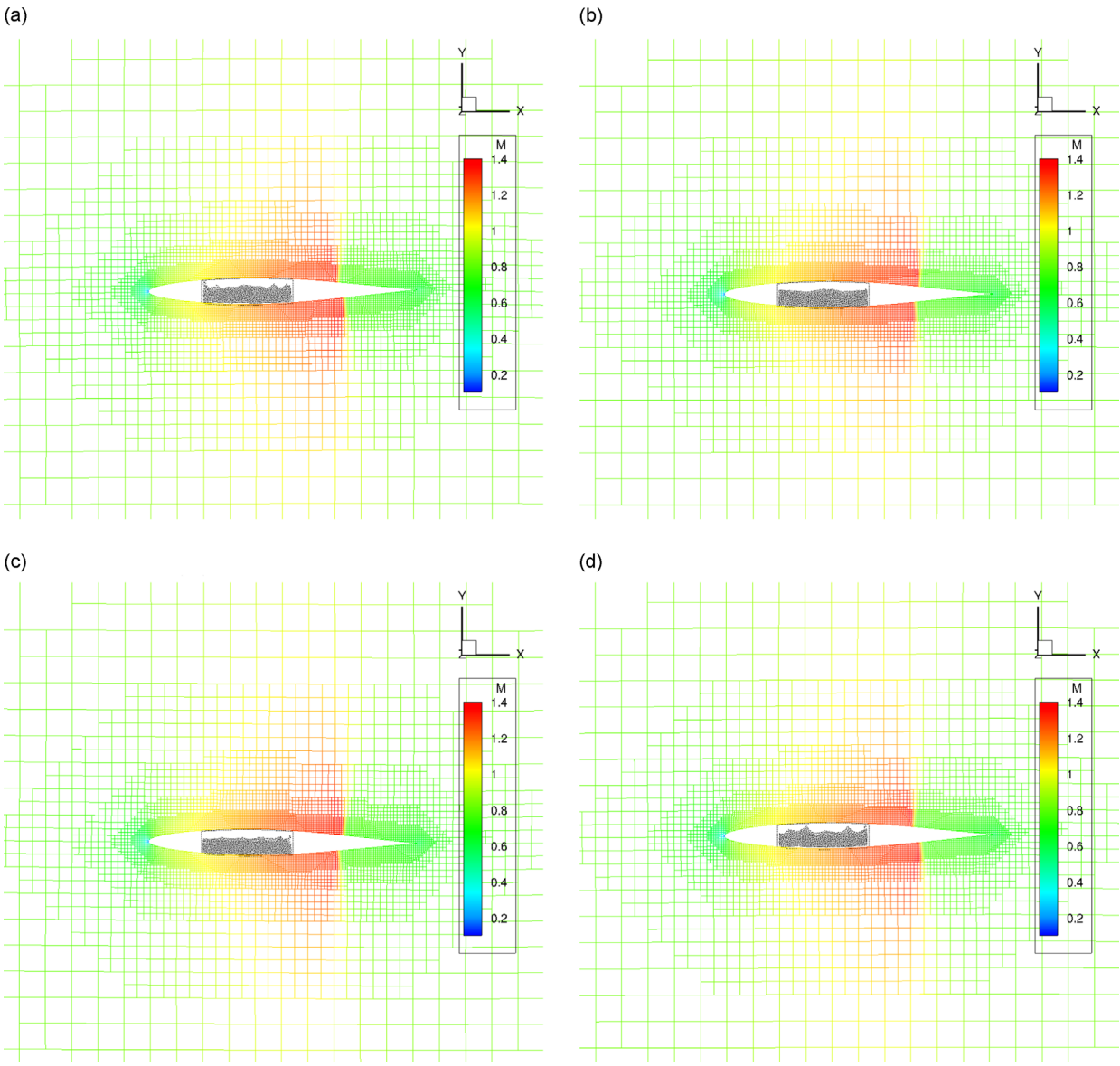

Fig. 11. System in motion, T_α is the torsional period, 67% fill. (a) $T = 2.5T_\alpha$, (b) $T = 5T_\alpha$, (c) $T = 7.5T_\alpha$, (d) $T = 10T_\alpha$.

sloshing reduced frequency $k_{sl} = \sqrt{\omega_\alpha^2 b/g}$ is implied that may be related to its aerodynamic equivalent by $k_{sl} = k_c V_\infty / \sqrt{bg}$. gb/c^2 is a ratio of characteristic speeds, as c is the speed of sound in the external flow and gb is proportional to the characteristic wave speed of shallow water waves.

4.1. Time marching

For time accurate aeroelastic simulation it is preferable to synchronise the fluid and structural equations every timestep. It is possible to solve both the fluid flow and the structural problem together using a monolithic scheme (Bendiksen, 1991; Blom, 1998), but this is impractical for many problems, lacks flexibility and limits application of the wealth of experience that exists in the computational fluid dynamics (CFD) and FE fields. It is more usual to apply the partitioned method (Piperno et al., 1995) and solve each of the fluid and structural domains separately using well established techniques for the field in question and then couple the solutions by the exchange of forces and displacements. In this work the partitioned scheme is used owing to these advantages and also the difficulty of envisaging a monolithic scheme where part of the solution is calculated using a meshless method and part using a mesh based method.

For strong coupling, sub-iteration is often used to achieve convergence over a timestep (Alonso and Jameson, 1994). In comparison, weak coupling alternates between structural and fluid calculations without regard for synchronisation (Farhat

and Lesoinne, 2000). A strongly coupled partitioned approach requires the exchange of information between solvers and this is an important and well studied problem with a number of methods for exchanging information across the different mesh geometries in each domain (de Boer et al., 2007; Farhat et al., 2003; Rendall and Allen, 2008). However, in this work the structural model is such that integration of forces around the boundary is sufficient for the transfer of information, but owing to the different timesteps the most important consideration is how force and displacement information is exchanged in time.

Three separate codes must be coupled together; the Euler code for the external aerodynamics, the structural code and the SPH for the internal fuel. The most natural way to do this is through the structural solver; forces on the aerofoil due to the aerodynamics and the internal fuel can be applied as source terms. Once Eq. (22) has been solved the pitch and plunge are communicated to the SPH and Euler codes which then adjust their boundary geometry.

However, due to the wall boundary condition (in the sense that a timestep integration must not move a particle through a wall) and the stiffness of the weakly compressible pressure/density relation the SPH code requires in general much smaller timesteps than the Euler or structural models. Typically the SPH timestep is in the region of ten or twenty times smaller than the Euler step, so to accommodate this mismatch a number of SPH timesteps are taken for each Euler step. During these substeps the fuel tank is forced in such a way that the position at one of these real substeps is calculated by a linear interpolation between the position at the Euler/structural timesteps, as shown in Fig. 3. The force coefficients are extracted from the SPH code only at the final substep.

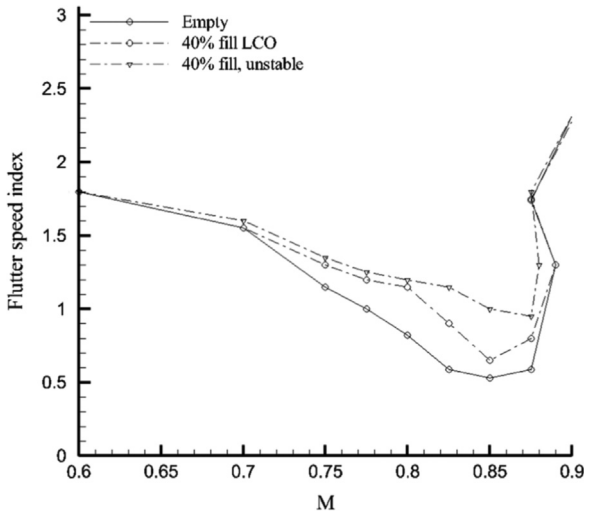

Fig. 12. Flutter boundary for 40% fill level.

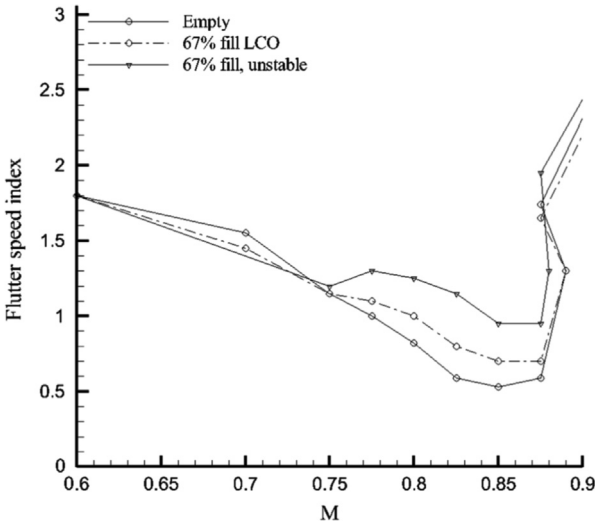

Fig. 13. Flutter boundary for 67% fill level.

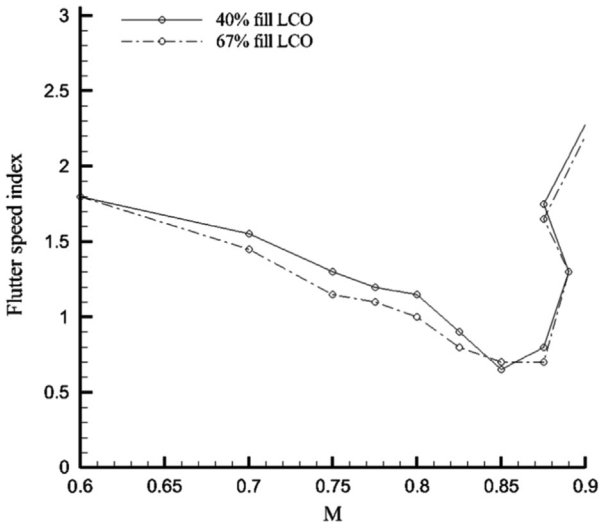

Fig. 14. Comparison of 40% and 67% fill levels.

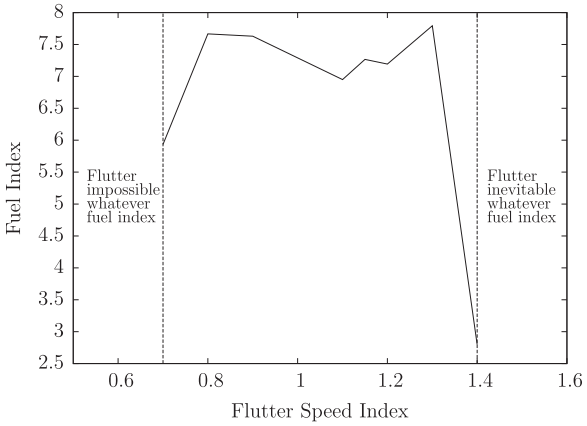

Fig. 15. Flutter boundary at $M=0.825$, 67% full tank, time marching.

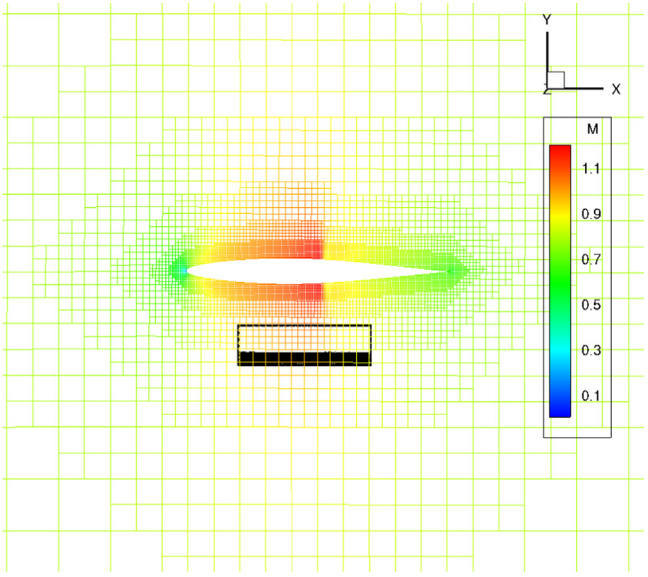

Fig. 16. Initial set up, external tank.

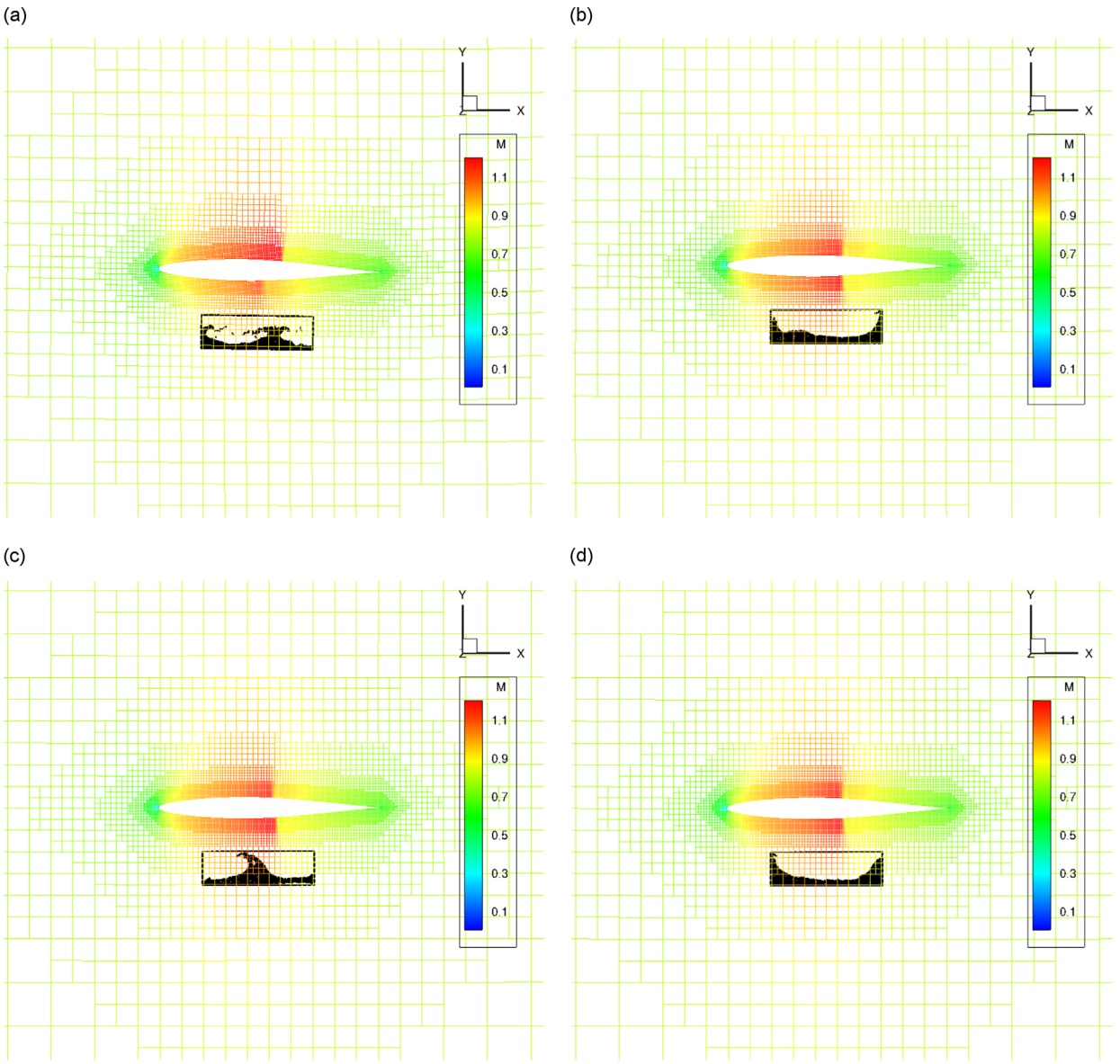

Fig. 17. System in motion, T_α is the torsional period, external tank, $M=0.85$. (a) $T=7.5T_\alpha$, (b) $T=15T_\alpha$, (c) $T=22.5T_\alpha$, (d) $T=30T_\alpha$.

The three solvers are therefore strongly coupled through iteration following the process outlined in Fig. 4. The SPH and Euler solvers are both advanced to the next timestep where the force coefficients on the structure are calculated. These force coefficients are then used to calculate new pitch and plunge positions at the end of the timestep, which are then communicated to the Euler and SPH solvers to iterate towards an improved solution. This process cycles until a convergence criterion is met after which the timestep advances; a solution is considered to be converged when the changes over each iteration in position, velocity and density are three orders of magnitude smaller than the initial change.

5. Validation

5.1. Sub-iteration of SPH tool

In order to validate the concept of running each model at a different timestep a comparison was made for a single time history, as shown in Fig. 5. The baseline was obtained by running the CFD code at every 16th SPH step, which means the CFD code is running at a smaller timestep than required for accuracy. Indeed, for this case the overhead in simulation time for running the CFD code at every 16th SPH timestep instead of every 64th SPH step was 312%. Little difference is seen as a

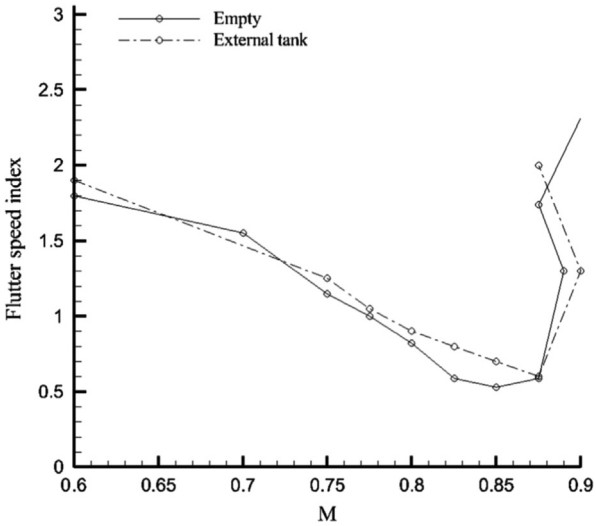

Fig. 18. Flutter boundary for external fuel tank, time-marching.

result of the larger Euler step, and so this technique allows the aerodynamic timestep to be set independently from the SPH timestep. Final simulations used 32 SPH steps per Euler step.

5.2. CFD-structure

Previous studies have been conducted using the two degree of freedom model used in this paper. Alonso and Jameson (1994) calculate a flutter boundary for the NACA-64A010 aerofoil using the structural parameters suggested by Isogai (1979) to model a swept back wing. Using the notation set out in Section 3 these are $\mu = 60$, $x_\alpha = 1.8$, $r_\alpha = 3.48$ and $\omega_h/\omega_\alpha = 1$.

To find the flutter boundary the aerofoil was given an initial impulsive angular velocity and the resulting time histories were examined to find the flutter index at which the perturbation began to grow. The flutter boundary produced using the time marching method presented in this work, and also using a p–k analysis (Hassig, 1971), is compared to Alonso and Jameson's (1994) in Fig. 6. The good agreement between the codes suggest that the flow–structure coupling scheme used here is accurate, while the slightly lower boundary prediction of the p–k analysis is consistent with a component of nonlinear damping from shock motion not being completely represented in the harmonic coefficients used in the p–k method.

5.3. SPH-structure

5.3.1. Numerical test

In order to provide a comparison between the fuelled and unfuelled systems that is independent of inertial effects, the total mass, moment of inertia and centre of mass of the wing and fuel at equilibrium are kept constant whatever the fuel fill level. This means for a full fuel tank the dynamics of the system will be very similar to the system with no fuel, and that if the fuel were to be 'frozen', the systems would be identical. Fig. 7 shows the comparison for the same initial perturbation from equilibrium. The system with a full, free-flowing fuel tank has a different initial transient and smaller amplitude compared to the original model. This is expected as the perturbation of the structure sets up flow in the fuel and damps the system reducing the amplitude.

5.3.2. Experimental comparison

To validate the SPH-structure coupled model, an experimental rig was constructed consisting of a hinged box. As shown in Fig. 8 the frame was built of aluminium sections, between which perspex panels were mounted and sealed to contain the water. The empty model mass and centre of mass location were measured and the moment of inertia found through comparison of the lumped mass frequency to the actual frequency, while damping in the bearing was characterised for the axle loads of interest here.

Tests were performed with the tank a fill level of $\frac{1}{8}$ and time histories measured for a range of starting amplitudes (5°, 10°, 15°, 20°, 25°, 30°) using an angular encoder. In this work, comparison is only made to the 20° starting amplitude case.

Fig. 9 illustrates experimental and numerical angular time histories. The SPH-structure model replicates the measured behaviour well, while the variations further on in the history at smaller amplitudes are likely to be linked to variability in the axle damping. Free surface shapes are compared in Fig. 8 at a series of different times during the motion, and the agreement is commensurate with that seen for rigid dam break simulations (Gomez-Gesteiraa et al., 2012).

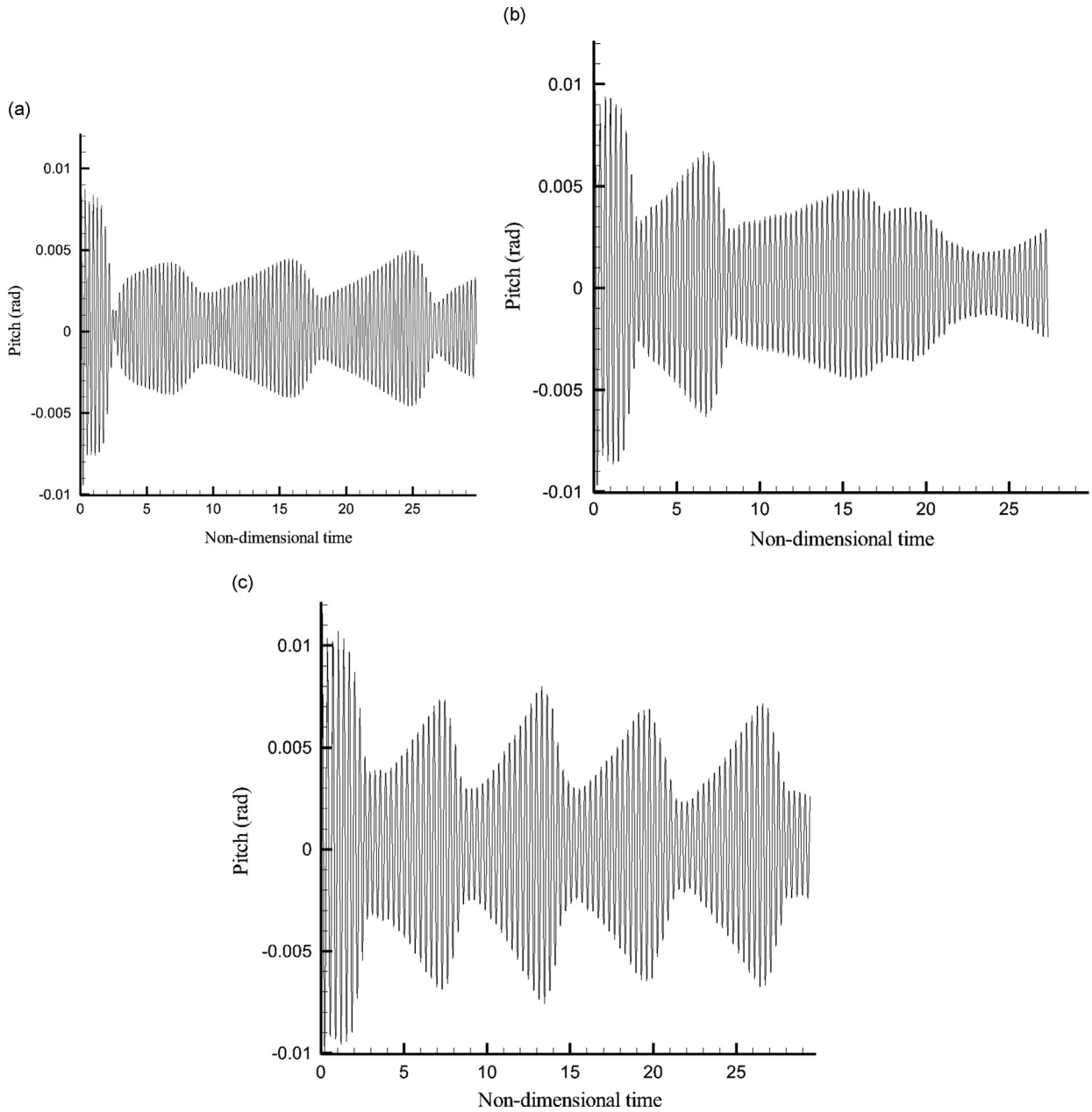

Fig. 19. Time histories for $M=0.825$ for external tank. (a) Speed index $=0.70$, (b) Speed index $=0.75$, (c) Speed index $=1.1$.

6. Results

For the following results $gb/c^2 = 5.435 \times 10^{-4}$ and $\rho_f/\rho_g = 833.3$. These values were chosen based upon reasonable values for a full scale aircraft, and the geometries of the internal and external cases were selected to be representative of aircraft configurations.

6.1. Internal tank

Tests were conducted at fill levels of 40% and 67% for an internal fuel tank in a NACA-64A010 aerofoil with structural parameters suggested by Isogai (1979) for a swept back wing. Fig. 10 shows the initial configuration of the test for 67% fill by depth. The fuel is held in the internal tank and the free stream Mach number is 0.85. Fig. 11 shows the system in motion at times given in terms of the pitching natural period.

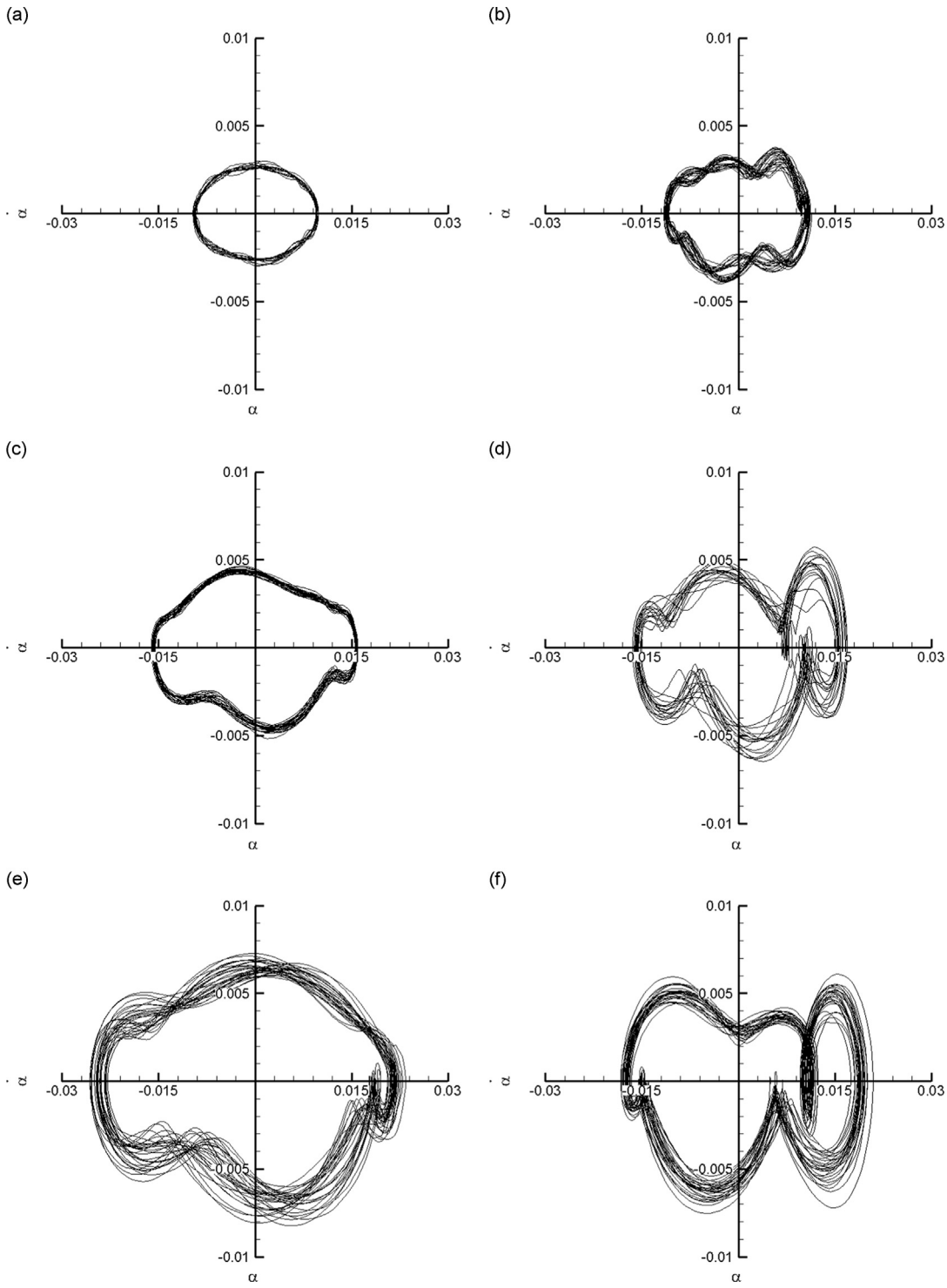

Fig. 20. Phase plots for $M=0.825$ at varying speed indices for 40% fill and 67% fill (clockwise loops). (a) Speed index = 0.8, 40% fill. (b) Speed index = 0.8, 67% fill. (c) Speed index = 0.95, 40% fill. (d) Speed index = 0.95, 67% fill. (e) Speed index = 1.1, 40% fill. (f) Speed index = 1.1, 67% fill.

Results in Figs. 12 and 13 share a similar trend. Addition of the fuel has the effect of raising the flutter boundary, especially for transonic Mach numbers, confirming an extra damping effect from the fuel motion, most likely as a consequence of $k_{sl}=kV_\infty/\sqrt{bg}$. An increase in the Mach number therefore increases the sloshing non-dimensional frequency relative to that of the aerodynamic system, which introduces higher damping from higher sloshing frequencies.

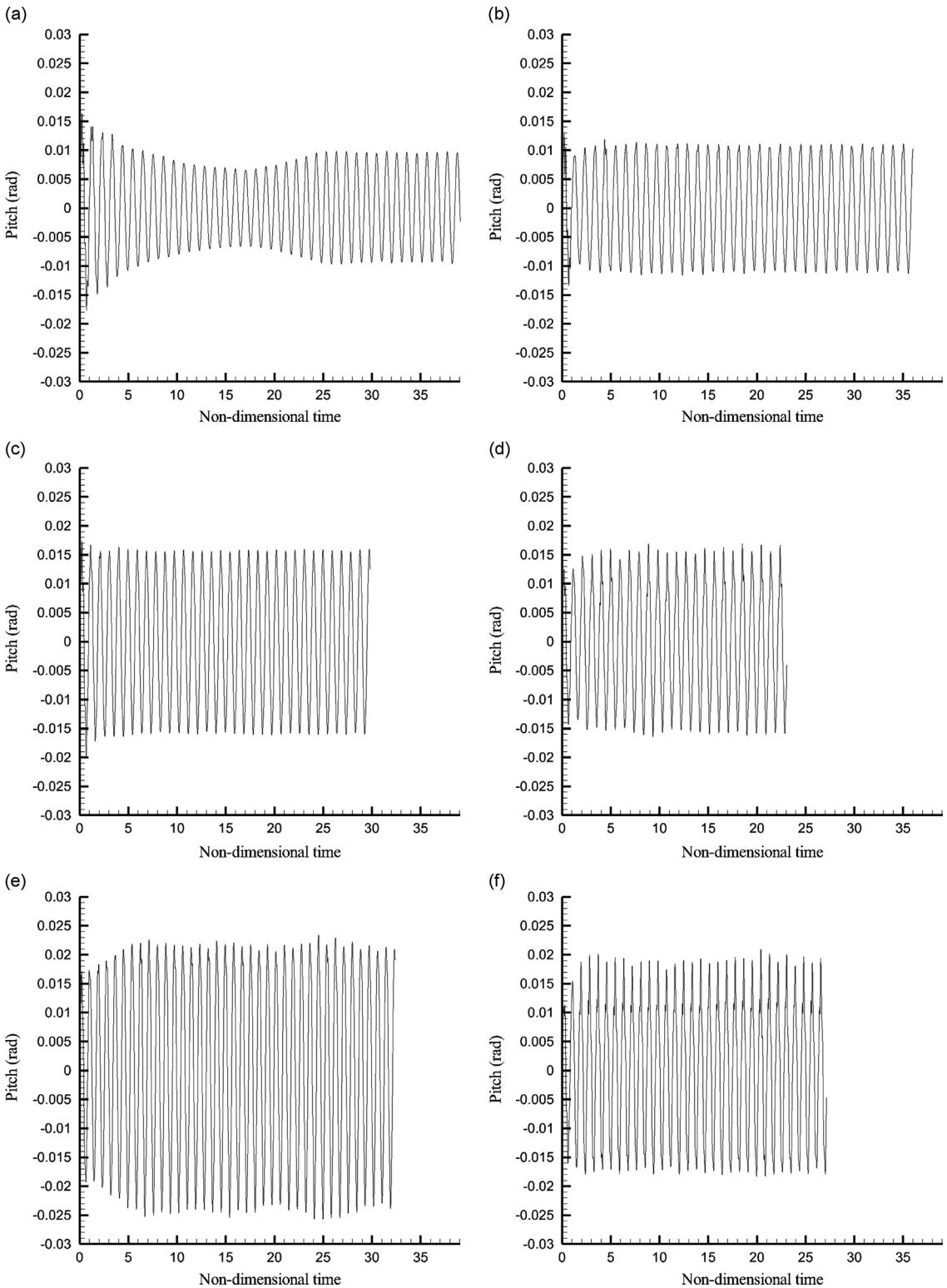

Fig. 21. Time histories for $M=0.825$ at varying speed indices for 40% fill and 67% fill. (a) Speed index=0.8, 40% fill. (b) Speed index=0.8, 67% fill. (c) Speed index=0.95, 40% fill. (d) Speed index=0.95, 67% fill. (e) Speed index=1.1, 40% fill. (f) Speed index=1.1, 67% fill.

An exception to this is shown in Fig. 13 for the 67% fill case, where a single point does exist with a lower flutter speed index. The conclusion is therefore consistent with Farhat et al. (2013) where it was determined that ignoring the fuel motion tends to underestimate flutter speeds, but exceptions, as noted, may exist in specific cases.

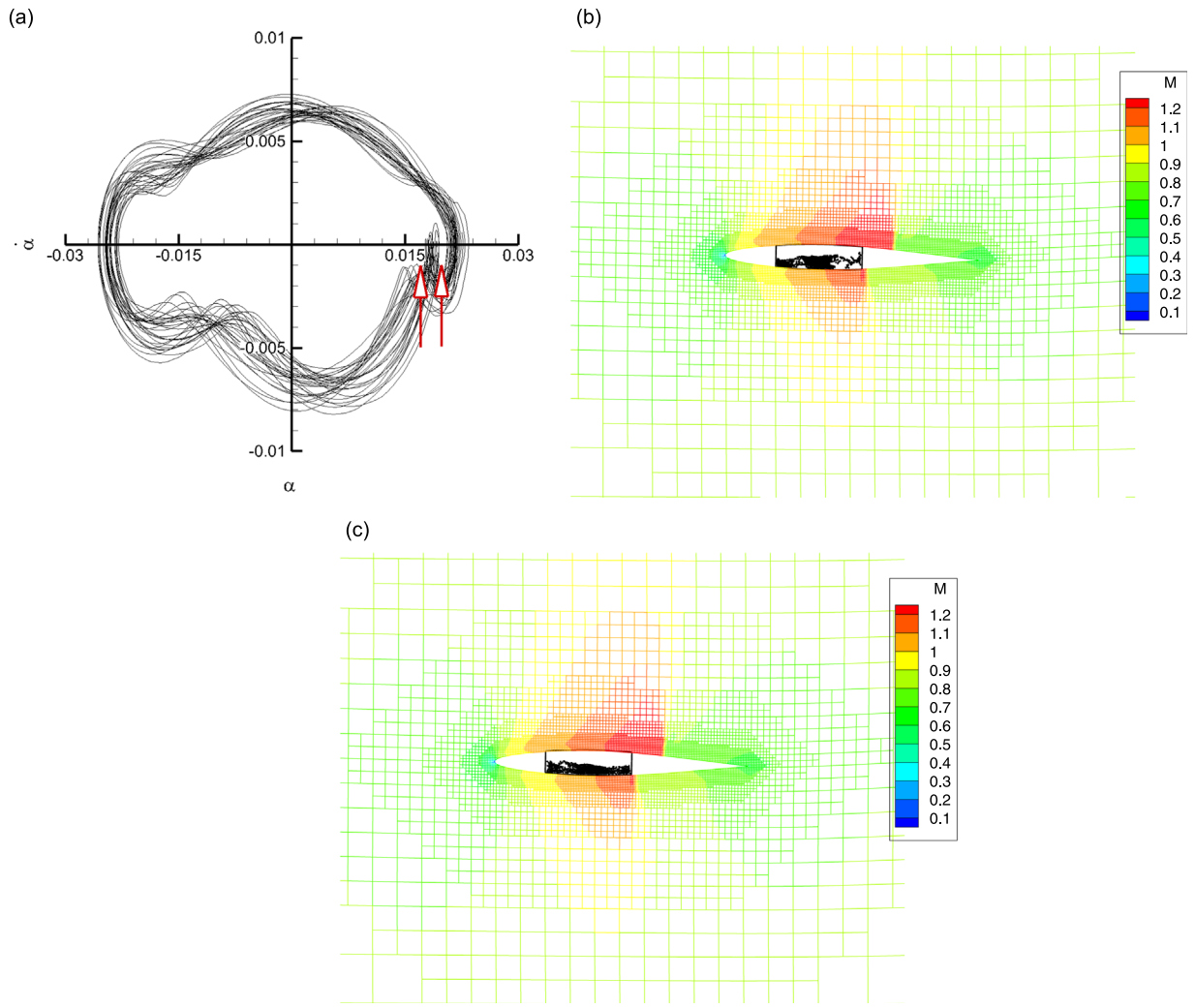

Fig. 22. Illustration of process driving phase plot turning points, for 40% fill. (a) Speed index = 1.1, 40% fill (clockwise loop). (b) Speed index = 1.1, 40% fill, shortly before phase plot turning point (right arrow) in Fig. 22(a), pre-slamming. Note elevation of fluid above tank floor. (c) Speed index = 1.1, 40% fill, shortly after phase plot turning point (left arrow) in Fig. 22(a), post-slamming.

In the case of the structure alone the system tends to go straight from stable to unstable as the flutter speed index is raised, however with fuel present Figs. 12 and 13 show that there is a large region where the system enters a limit cycle, giving a softer stability crossing. This may be due to the fuel damping effect increasing as the motions become more violent. Of the two fill levels, Fig. 14 shows that the 67% level is slightly less stable, possibly as a consequence of a larger component of the mass being able to move freely as fuel.

The variation of the flutter boundary with different values of the fuel index defined in Section 4 was studied for the internal case. Results are shown in Fig. 15 for a fixed external Mach number of 0.825. The graph shows that for this Mach number the critical fuel index remains nearly constant over a range of flutter speed index values. For both high and low flutter speed indices the fuel index at flutter is greatly and abruptly reduced and past the point shown in Fig. 15 the system is either unconditionally stable with variation in fuel index or unconditionally unstable and as such, no flutter boundary exists.

6.2. External tank

A 30% full external fuel tank of the under wing type was also considered. Again the NACA-64A010 aerofoil was used with the same structural parameters. The aerodynamic effects of the fuel tank were not considered; it only interacted with the wing through the forces due to the fuel inside. The tank was 30% full. Fig. 16 shows the initial set up for a free stream Mach number of 0.8 and Fig. 17 shows snapshots in time of the system in motion.

The time marching method for establishing the flutter boundary was used and Fig. 18 shows the flutter boundary obtained. Fig. 18 suggests a damping effect which is on the whole is less than for the internal tank, while behaviour of the

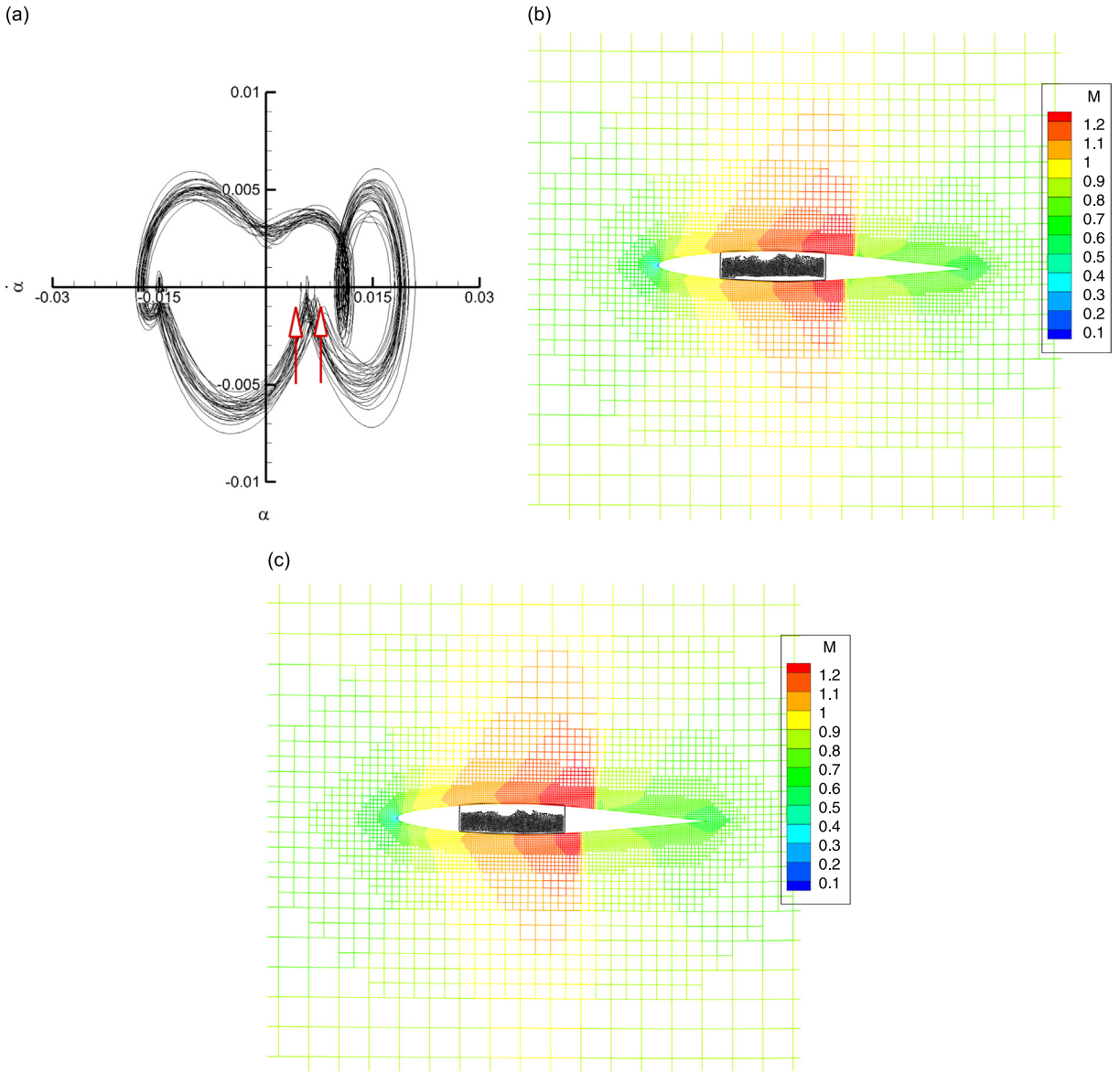

Fig. 23. Illustration of process driving phase plot turning points, for 67% fill. (a) Speed index = 1.1, 67% fill (clockwise loop). (b) Speed index = 1.1, 67% fill, shortly before phase plot turning point (right arrow) in Fig. 23(a), pre-slamming. Note elevation of fluid above tank floor. (c) Speed index = 1.1, 67% fill, shortly after phase plot turning point (left arrow) in Fig. 23(a), post-slamming.

system as it becomes unstable is also different. In the internal tank case as the flutter speed index increases the system reaches a limit cycle, which it retains as the speed index increases further, until finally becoming fully unstable and experiencing growth. When the external tank is used the system is stable until the flutter boundary, at which point the beating type phenomenon shown in Fig. 19 is seen together with a larger region of limit cycles. This beating indicates that there are two frequency components that are close together, which both influence the motion. A probable cause is the interaction between vertical fluid motion and surface wave motion; when the system is beating the minima of the amplitude envelope coincide with wave impacts on the tank top.

7. Further analysis of motion characteristics

Fig. 20 shows the $\dot{\alpha}$ vs. α phase plots for the two internal tank cases at varying speed indices. The initial limit cycle is clear in Fig. 20(a) and (b), and as the speed index grows these LCOs expand and assume a more complicated structure. This takes place because the increase in speed index raises the aerodynamic forcing in comparison to the spring stiffness, and excites more violent motions of the contained fuel. A key change appears when the accelerations of the motion approach gravity, and the fuel moves away from the walls. The subsequent slamming impacts between the fuel and walls lead to

Table 1
Largest Lyapunov exponents for varying fill levels (internal tank). 'NC' indicates a non-chaotic result.

Flutter speed index	Empty	40%	67%
0.80	NC	NC	NC
0.85	NC	NC	NC
0.90	NC	NC	NC
0.95	NC	NC	NC
1.00	NC	NC	3.85×10^{-3}
1.05	NC	4.68×10^{-3}	3.62×10^{-3}
1.10	NC	4.77×10^{-3}	7.56×10^{-3}

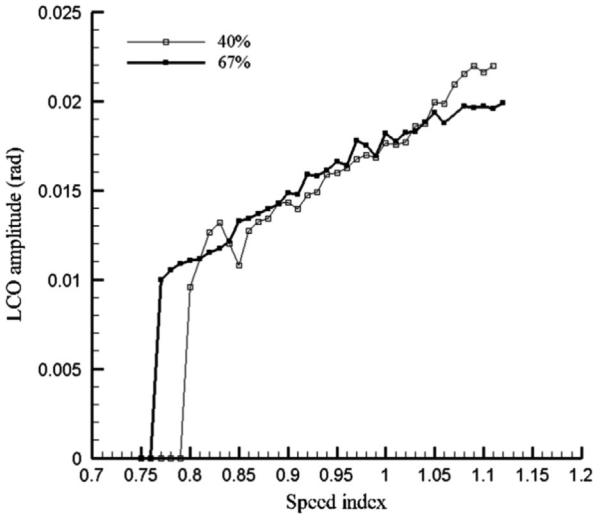

Fig. 24. Amplitude of LCO vs. speed index for 40% and 67% internal fill cases for $M=0.825$.

nonlinear behaviour with large, abrupt changes in the forces, and thus the turning points in the phase plots (Figs. 20(e) and (f)). The time histories for these plots shown in Fig. 21 reveal that the turning points are linked to rapid changes in the motion near the peak amplitudes, which is when the the acceleration crosses through gravity and slamming is likely. Figs. 22 and 23 confirm the link to slamming behaviour, as time snapshots just before and just after show clear pre-slamming and post-slamming configurations of the fuel.

To help assess the nature of these motions the largest Lyapunov exponents were calculated using the technique of Rosenstein et al. (1993). This approach identifies a log-linear region in the divergence of nearby trajectories plotted against time. For some of the LCOs no log-linear region was observable, indicating non-chaotic behaviour, but for the higher speed indices positive exponents were found, indicating a chaotic system. As shown in Table 1, these ranged from a low of 3.62×10^{-3} up to 7.56×10^{-3}. The presence of a chaotic response would be consistent with the more intricate phase plots, and can be attributed to the slamming behaviour of the fuel.

The amplitude of the LCOs was also explored across the speed index range for the 40% and 67% internal fill cases at $M=0.825$, as shown in Fig. 24. Once the flutter boundary is crossed, LCO amplitude increases as the speed index is raised further. Since the LCO behaviour does not always yield a response of constant amplitude (see phase plots of Fig. 20), clear identification of a single amplitude is not possible and this accounts for the element of noise in Fig. 24. The 67% fill case shows a lower flutter point, but the amplitude growth with speed index is very similar for both fill levels, except at the higher speed indices which begin to approach the point of unconstrained growth.

8. Conclusions

An SPH code, a structural model and an external aerodynamics solver have been developed and coupled in a time-accurate fashion. This multi-physics technique allows the non-linear behaviour of the fuel, such as wave breaking and tank top impacts during aeroelastic motion, to be modelled, along with the effects of that fuel motion on aeroelastic behaviour. A flutter boundary has been calculated for different fuel fill levels and it is seen that the addition of fuel usually raises the flutter boundary even when the effect of the fuel added mass is neglected (see also Farhat et al., 2013). Additionally, a region where the system enters a limit cycle is observed. A contrast is also seen between an internal and external tank; the external tank provides less damping than the internal tank. A beating type time history is seen in the limit cycle region of the

external tank response and it is suggested that this is due to an interaction between the vertical and horizontal fluid motion. It can be seen that there is a critical fuel index value that leads to flutter instabilities.

The time marching technique used here is robust and can easily be applied to many geometries of tank including ones with complex baffle configurations. Practical fuel tanks will not have such a simple geometry and allowing the fuel to move in an unrestrained manner may cause high impact loads or stability problems. Future work will therefore consider evaluating a range of tank and baffle geometries for internal and external arrangements.

Acknowledgements

This work was carried out using the computational facilities of the Advanced Computing Research Centre, University of Bristol – http://www.bris.ac.uk/acrc/. James Hall is funded by EPSRC doctoral training account EP/K502996/1. A full dataset for the sloshing experiment is available on request.

References

Abramson, H.N., 1966. The dynamic behavior of liquids in moving containers, with applications to space vehicle technology. Report SP-106, NASA.
Allen, C.B., Taylor, N.V., Fenwick, C., Gaitonde, A., Jones, D., 2005. A comparison of full non-linear and reduced order aerodynamic models in control law design for active flutter suppression. International Journal for Numerical Methods in Engineering 64 (12) (December), 1628–1648.
Alonso, J.J., Jameson, A., 1994. Fully-implicit time-marching aeroelastic solutions. In: 32nd Aerospace Sciences Meeting and Exhibit, AIAA, Reno. http://dx.doi.org/10.2514/6.1994-56. 1994-56.
Banim, R., Lamb, R., Bergeon, M., 2006. Smoothed particle hydrodynamics simulation of fuel tank sloshing. In: 25th International Congress of the Aeronautical Sciences.
Bauer, H., 1963. Stability boundaries of liquid-propelled space vehicles with sloshing. AIAA Journal 1 (4), 1583–1589.
Bendiksen, O.O., 1991. A new approach to computational aeroelasticity. In: AIAA/ASME/ASCE/AHS/ASC 32nd Structures, Structural Dynamics, and Materials Conference, vol. 3.
Blom, F.J., 1998. A monolithical fluid–structure interaction algorithm applied to the piston problem. Computer Methods in Applied Mechanics and Engineering 167, 369–391.
Cole, R.H., 1948. Underwater Explosions. Princeton University Press, Princeton.
de Boer, A., van Zuijlen, A.H., Bijl, H., 2007. Review of coupling methods for non-matching meshes. Computer Methods in Applied Mechanics and Engineering 196 (8), 1515–1525.
Djayapertapa, L., Allen, C.B., 2001. Aeroservoelastic simulation by time-marching. Aeronautical Journal 105 (1054), 667–678.
Djayapertapa, L., Allen, C.B., Fiddes, S., 2001. Two-dimensional transonic aeroservoelastic computations in the time domain. International Journal for Numerical Methods in Engineering 52 (December (12)), 1355–1377.
Farhat, C., Lesoinne, M., 2000. Two efficient staggered algorithms for the serial and parallel solution of three-dimensional nonlinear transient aeroelastic problems. Computer Methods in Applied Mechanics and Engineering 182 (3-4), 499–515, http://dx.doi.org/10.1016/S0045-7825(99)00206-6. URL ⟨http://www.sciencedirect.com/science/article/pii/S0045782599002066⟩.
Farhat, C., Geuzaine, P., Brown, G., 2003. Application of a three-field nonlinear fluid–structure formulation to the prediction of the aeroelastic parameters of an F-16 fighter. Computers and Fluids 32 (1), 3–29.
Farhat, C., Chiu, E., Amsallem, D., Schott, J., Ohayon, R., 2013. Modeling of fuel sloshing and its physical effects on flutter. AIAA Journal 51 (June (9)), 2252–2265, http://dx.doi.org/10.2514/1.J052299.
Ferman, M., Unger, W., 1979. Fluid–structure interaction dynamics in aircraft fuel tanks. AIAA Journal 16 (12), 885–890.
Firouz-Abadi, R.D., Zarifian, P., Haddadpour, H., 2012. Effect of fuel sloshing in the external tank on the flutter of subsonic wings. Journal of Aerospace Engineering. http://dx.doi.org/10.1061/(ASCE)AS.1943-5525.0000261.
Geuzaine, P., Brown, G., Harris, C., Farhat, C., 2003. Aeroelastic dynamic analysis of a full F-16 configuration for various flight conditions. AIAA Journal 41 (March (3)), 363–371.
Gingold, R.A., Monaghan, J.J., 1977. Smoothed particle hydrodynamics: theory and application to non-spherical stars. Monthly Notices of the Royal Astronomical Society 181, 375–389.
Gomez-Gesteiraa, M., Rogers, B., Crespo, A., Dalrymple, R., Narayanaswamy, M., Domingueza, J., 2012. Sphysics development of a free-surface fluid solver. Part1: theory and formulations. Computers and Geosciences 48, 289–299.
Hassig, H., 1971. An approximate true damping solution of the flutter equation by determinant iteration. AIAA Journal 8 (11), 885–889.
Hirt, C.W., Nichols, B., 1981. Volume of fluid (VOF) method for the dynamics of free boundaries. Journal of Computational Physics 39, 201–225.
Hirt, C., Amsden, A., Cook, J., 1974. An arbitrary Lagrangian–Eulerian computing method for all flow speeds. Journal of Computational Physics 14 (3), 227–253, http://dx.doi.org/10.1016/0021-9991(74)90051-5. URL ⟨http://www.sciencedirect.com/science/article/pii/0021999174900515⟩.
Hubner, B., Walhorn, E., Dinkler, D., 2004. A monolithic approach to fluid–structure interaction using space–time finite elements. Computer Methods in Applied Mechanics and Engineering 193, 2087–2104.
Huebner, K.H., Byrom, T.G., Thornton, E.A., 1995. The Finite Element Method for Engineers, 3rd ed. John Wiley & Sons, Wiley.
Isogai, K., 1979. On the transonic-dip mechanism of flutter of a sweptback wing. AIAA Journal 17 (7), 793–795.
Isogai, K., 1980. Numerical Study of Transonic Flutter of a Two-dimensional Airfoil. Technical Report TR-617T. National Aerospace Laboratory of Japan. URL ⟨http://repository.tksc.jaxa.jp/pl/dr/NALTR0617T000/en⟩.
Jameson, A., Schmidt, W., Turkel, E., 1981. Numerical solution of the Euler equations by finite volume methods using Runge Kutta time stepping schemes. In: Fluid Dynamics and Co-located Conferences. 1981, American Institute of Aeronautics and Astronautics, Reno. URL http://dx.doi.org/10.2514/6.1981-1259.
Kim, Y., Nam, B.W., Kim, D.W., Kim, Y.S., 2007. Study on coupling effects of ship motion and sloshing. Ocean Engineering 34, 2176–2187.
Lee, E.S., Moulinec, C., Xu, R., Violeau, D., Laurance, D., Stansby, P., 2008. Comparisons of weakly compressible and truly incompressible algorithms for the SPH mesh free particle method. Journal of Computational Physics 227 (18), 8417–8436.
Lee-Rausch, E.M., Batina, J.T., 1993. Calculation of the AGARD Wing 445.6 Flutter using Navier–Stokes Aerodynamics, AIAA Paper No. 93-3476.
Liu, G.R., Liu, M.B., 2005. Smoothed Particle Hydrodynamics: A Meshfree Particle Method. World Scientific Publishing Co..
Lucy, L.B., 1977. A numerical approach to the testing of the fission hypothesis. Astronomical Journal 82 (12), 1013–1024.
Maman, N., Farhat, C., 1995. Matching fluid and structure meshes for aeroelastic computations: a parallel approach. Computers and Structures 54 (4), 779–785.
Merten, K., Stephenson, B., 1952. Some Dynamic Effects of Fuel Motion in Simplified Model Tip Tanks on Suddenly Excited Bending Oscillations. Technical Report TN 2789, NACA.
Monaghan, J.J., 1988. An introduction to SPH. Computer Physics Communications 48 (1), 89–96.

Monaghan, J.J., 1994. Simulating free surface flows with SPH. Journal of Computational Physics 110, 399–406.
Morris, J.P., Fox, P.J., Zhu, Y., 1997. Modeling low Reynolds number incompressible flows using SPH. Journal of Computational Physics 136, 214–226.
Peterson, L., Crawley, E., Hansman, R.J., 1989. Nonlinear fluid slosh coupled to the dynamics of a spacecraft. AIAA Journal 27 (9), 1230–1240.
Piperno, S., Farhat, C., 2001. Partitioned procedures for the transient solution of coupled aeroelastic problems—Part II: energy transfer analysis and three-dimensional applications. Computer Methods in Applied Mechanics and Engineering 190 (24–25), 3147–3170.
Piperno, S., Farhat, C., Larrouturou, B., 1995. Partitioned procedures for the transient solution of coupled aeroelastic problems—Part I: model problem, theory and two-dimensional application. Computer Methods in Applied Mechanics and Engineering 124 (1–2), 79–112.
Price, D.J., 2012. Smooth particle hydrodynamics and magnetohydrodynamics. Journal of Computational Physics 231, 759–794.
Rebouillat, S., Liksonov, D., 2010. Fluid–structure interaction in partially filled liquid containers: a comparative review of numerical approaches. Computers and Fluids 39 (5), 739–746.
Rendall, T.C.S., Allen, C.B., 2008. Unified fluid–structure interpolation and mesh motion using radial basis functions. International Journal for Numerical Methods in Engineering 74 (10), 1519–1559.
Rosenstein, M., Collins, J., Luca, C.J.D., 1993. A practical method for calculating the largest Lyapunov exponents from small data sets. Physica D 65 (December), 117–134.
Sankar, S., Ranganathan, R., Rakheja, S., 1992. Impact of dynamic fluid slosh loads on the directional response of tank vehicles. Vehicle System Dynamics 21 (6), 385–404.
Saturn Flight Evaluation Working Group, 1961. Saturn SA-1 flight evaluation. Technical Report MPR-SAT-WF-61-8, NASA.
Sewall, J.L., 1957. An Experimental and Theoretical Study of the Effect of Fuel on Pitching-Translation Flutter. Technical Note 4166, NACA.
Slabinski, V.J., 1978. INTELSAT IV in-orbit liquid slosh tests and problems in the theoretical analysis of the data. In: Flight Mechanics/Estimation Theory Symposium, pp. 183–221.
Souto-Iglesias, A., Delormea, L., Peŕez-Rojasa, L., Abril-Peŕezb, S., 2006. Liquid moment amplitude assessment in sloshing type problems with smoothparticle hydrodynamics. Ocean Engineering 39 (5), 1462–1484.
Taylor, N.V., Allen, C.B., Gaitonde, A., Jones, D., 2004. A structure-coupled CFD method for time marching flutter analysis. Aeronautical Journal 108 (1086) (August), 389–401.
Vreeburg, J., 2005. Measured states of sloshsat FLEVO. In: 56th International Astronautical Congress.
Wendland, H., 1995. Piecewise polynomial, positive definite and compactly supported radial functions of minimal degree. Advances in Computational Mathematics 4, 389–396.
Woodgate, M.A., Badcock, K.J., Rampurawala, A.M., Richards, B.E., 2005. Aeroelastic calculations for the Hawk aircraft using the Euler equations. Journal of Aircraft 42 (July–August (4)), 1005–1011.